Provided by the author(s) and University of Galway in accordance with publisher policies. Please cite the published version when available.

Title	Experimental and computational investigation of the role of stress fiber contractility in the resistance of osteoblasts to compression
Author(s)	McGarry, J. Patrick; Weafer, Paul; Jarvis, S. P.; Ronan, William
Publication Date	2013
Publication Information	Weafer, PP,Ronan, W,Jarvis, SP,McGarry, JP (2013) 'Experimental and Computational Investigation of the Role of Stress Fiber Contractility in the Resistance of Osteoblasts to Compression'. Bulletin Of Mathematical Biology, 75 :1284-1303.
Link to publisher's version	http://dx.doi.org/10.1007/s11538-013-9812-y
Item record	http://hdl.handle.net/10379/4107
DOI	http://dx.doi.org/http://dx.doi.org/10.1007/s11538-013-9812-y

Downloaded 2024-03-20T08:33:38Z

Some rights reserved. For more information, please see the item record link above.

Experimental and computational investigation of the role of stress fiber contractility in the resistance of osteoblasts to compression

P. P. Weafer,[1]* W. Ronan,[1]* S. P. Jarvis,[2] and J. P. McGarry[1a]

[1]Department of Mechanical and Biomedical Engineering,
National University of Ireland, Galway,
Ireland

[2]Nanoscale Function Group,
Conway Institute of Biomolecular and Biomedical Research,
University College Dublin,
Ireland

* Joint first authors

[a] Corresponding author:
Patrick McGarry
Department of Mechanical and Biomedical Engineering
National University of Ireland, Galway
Ireland
Phone: +353 (0) 91 493165
Fax: +353 (0) 91 563991
E-Mail: patrick.mcgarry@nuigalway.ie

Abstract

The mechanical behavior of the actin cytoskeleton has previously been investigated using both experimental and computational techniques. However, these investigations have not elucidated the role the cytoskeleton plays in the compression resistance of cells. The present study combines experimental compression techniques with active modeling of the cell's actin cytoskeleton. A modified atomic force microscope is used to perform whole cell compression of osteoblasts. Compression tests are also performed on cells following the inhibition of the cell actin cytoskeleton using cytochalasin-D. An active bio-chemo-mechanical model is employed to predict the active remodeling of the actin cytoskeleton. The model incorporates the myosin driven contractility of stress fibers via a muscle-like constitutive law. The passive mechanical properties, in parallel with active stress fiber contractility parameters, are determined for osteoblasts. Simulations reveal that the computational framework is capable of predicting changes in cell morphology and increased resistance to cell compression due to the contractility of the actin cytoskeleton. It is demonstrated that osteoblasts are highly contractile and that significant changes to the cell and nucleus geometries occur when stress fiber contractility is removed.

Keywords:

in-vitro cell compression, active stress fiber model

1 Introduction

Mechanical loading is necessary for the healthy function of many cell types. For instance, mechanical deformation is considered essential for bone remodeling [1]. The response of osteoblasts to mechanical signaling is attributed to deformation of the cell and surrounding matrix [2][3]. Previous studies have shown that compressive loading induces mineralization of osteoblastic cells [4] and is an effective up-regulator of osteogenesis [5]. Furthermore, static and dynamic compression of chondrocytes has been shown to effect the regulation of type II collagen and aggrecan gene expression [6]. While the role of mechanical loading on cell function has been reported, the basic bio-mechanisms underlying these cellular mechanosensitive responses are still not fully understood. In order to elucidate the effect of mechanical loading on cell function it is essential to accurately characterize the mechanical behavior of the cell and its nucleus.

The use of whole cell compression testing to determine mechanical properties was initially reported by Thoumine et al. in which fibroblasts were compressed between two parallel plates to examine cell viscoelasticity [7]. Parallel plate compression was also used by Caille et al. in order to characterize the elastic properties of endothelial cells and their isolated nuclei [8]. Similar studies have been performed by Ofek et al. on chondrocytes [9] and Peeters et al. on myoblasts [10]. Typically, cell compression experiments are performed by seeding cells on stiff substrates. A flexible probe that is initially parallel to the substrate is used to impart a compressive deformation on the cell. By observing the deflection of the probe using a microscope, the compressive force can be computed using beam theory. The accuracy of such force measurements are typically in the range of 1-10 nN. Additionally, the nominal strain imparted on the cell cannot be accurately controlled due to significant deflections of the flexible probe during compression. Atomic force microscopy (AFM) has also been widely used to measure the resistance of cells to deformation. AFM systems can accurately measure forces of the order of pico-Newton. Additionally, sub-nanometer displacements can be accurately applied to cells. However, previous implementations of AFM based force spectroscopy for the mechanical characterization of cells have used sharp nano-scale probes which apply a highly localized deformation to the cell membrane. Such an approach suffers from a number of setbacks: applied deformations are restricted to the upper surface of the cell; measured forces are highly influenced by cell inhomogeneity; large deformations occur in a highly localized region of the cell, making it difficult to characterize the strain field and to interpret measured forces. In an effort to overcome these problems Lulevich et al. attached a sphere of diameter

40 µm to the end of the AFM cantilever [11]. In the present study a sphere of diameter 150 µm is attached to an AFM cantilever in order to perform whole cell compression of osteoblasts. This large sphere provides an approximately planar surface for whole cell compression. This system offers an advantage over previous parallel plate compression devices given the high level of precision offered by the modified AFM system for control of the nominal cell strain and for measurement of resultant compression forces.

Finite element simulation of cell compression experiments has been performed in order to determine cell elastic properties. Using a hyperelastic incompressible material model Caille et al. suggests that spread endothelial cells have a higher apparent stiffness than round cells [8]. This finding is also supported by the study of Darling et al. for mesenchymal stem cells (MSCs), osteoblasts, chondrocytes and adipocytes [12]. The finite element simulations of McGarry and McHugh [13] and McGarry [14] demonstrate that the apparent stiffness of spread cells must be artificially increased in order to capture the response of cells to compression and shear deformation. Experimental staining of sub-cellular structures reveal that remodeling of the actin cytoskeleton occurs during cell spreading. In order to elucidate the role of the actin cytoskeleton in the resistance of cells to compression it is necessary to simulate cell compression experiments using a modeling framework that predicts the distribution and contractility of the actin cytoskeleton.

The mechanical role of the cytoskeleton has previously been investigated by including contractility as a prescribed thermal strain or as predefined passive filaments [15][16]. However, these formulations do not consider the active contractility and the evolving distributions of stress fibers (SFs) in the cytoplasm. A previous study has proposed a novel computational model of contractile SF behavior based on the biochemistry of SF formation [17]. This active bio-chemo-mechanical model predicts the active remodeling of the actin cytoskeleton in terms of SF distribution and also incorporates the myosin driven contractility of SFs via a muscle-like constitutive law. This formulation has been used successfully to simulate cells on patterned substrates and cells adhered to arrays of microposts [18][19]. Recently, this study has been expanded into a fully 3D framework that allows for the simulation of realistic cell geometries and the inclusion of a separately modeled nucleus [20].

In the present study a modified AFM system is used to perform whole cell compression of osteoblasts [21]. Compression tests are also performed on cells following the inhibition of cell contractility. Additionally, cytoplasm and nucleus geometries are observed. A bio-chemo-mechanical model is used to simulate the remodeling and contractility of the actin cytoskeleton [20][22]. This active framework is placed in parallel with a passive hyperelastic material model which represents the non-contractile components of the cell cytoplasm. A detailed model calibration reveals that the computational framework is capable of simulating changes in cell morphology and increased resistance to cell compression due to the contractility of the actin cytoskeleton.

2 Materials and Methods

2.1 Experimental setup

Monotonic cell compression was performed by attaching a large sphere to the end of a tipless AFM cantilever, previously described by Weafer et al. [21], as shown in Figure 1. Briefly, a Ø 150 µm glass microsphere (Whitehouse Scientific) was attached to the end of a tipless cantilever (Lever F, NSC12/Tipless/AlBS, $k \approx 0.65$ N/m, MikroMasch). A two part epoxy (Loctite, Henkel Corp.) was used to attach the sphere to the leading edge of a cantilever using a combined micro-manipulation/optical microscope setup. Scanning electron microscopy, with a customized sample stage, verified microsphere positioning on the leading cantilever edge post-attachment.

The cantilever spring constant of the sphere-cantilever assemblage, k, was calculated according to the added mass method [23]. Spring constant values ranged from 0.3 - 0.5 N/m and were within 20 % of the values obtained for cantilevers prior to sphere attachment, obtained via the thermal method [24].

2.2 Monotonic cell compression

MC3T3-E1 osteoblasts (ATCC-LGC Standards) were cultured according to the method described by McGarry et al. [25]. Prior to experiments, cells were seeded at a single cell level on sterile glass coverslips, placed in tissue culture dishes and allowed to spread for 24 hours. The coverslip to which the cells were adhered was then placed within a BioHeater™ (Asylum Research) which was in turn secured to the stage of the Asylum Research MFP-3D atomic force microscope (AFM). Experiments were performed at 37 °C with cells remaining immersed in culture medium for the duration of the experiments.

Cell height was determined as the difference between the point of contact for force-displacement curves taken on the glass substrate beside a cell and those taken over the cell of interest [26]. Phase contrast optical microscopy allowed aligning of the microsphere above the center of the cell. Images were taken for each cell to measure cell base area. Each cell (untreated) was then subjected to a monotonic compression at a constant velocity (1.4 µm/s) until a compressive strain of 0.6 was achieved (compressive strain = (change in cell height / undeformed cell height)). When the velocity was increased to 4.3 µm/s no statistically significant change in compression force was observed, demonstrating that rate dependent viscoelastic effects are not evident at the loading rates considered in the study. The actin cytoskeleton was disrupted using 10 µM Cytochalasin D (Cyto-D) for 30 minutes. Following this, compression was repeated for the same cells (referred to hereafter as “Cyto-D cells”). In each case, force-strain curves and cell morphology was recorded, n = 11. Statistical differences were determined using Student’s paired t-tests. All data is presented as mean ± standard deviation.

2.3 Cytoskeleton morphology analysis

Cell samples were stained using an actin cytoskeleton and focal adhesion staining kit (Chemicon) following fixation with 4 % paraformaldehyde. Briefly, an anti-vinculin primary antibody conjugated to a FITC-conjugated secondary antibody and rhodamine-conjugated phalloidin were used to label focal adhesions and F-actin, respectively. Cells were also counterstained using DAPI. DAPI, FITC, and rhodamine were excited at 402, 488, and 561 nm, respectively. Emitted fluorescence appeared at 470, 525, and 590 nm for each fluorophore. Z-stacks of control cells (n = 5) and Cyto-D cells (n = 7) were acquired using a Nikon A1 confocal microscope with intervals of 200 nm between z-stack steps. The Nikon NIS-Elements AR 3.0 software package was used to quantify cytoskeletal and cell morphology details. Statistical differences were determined using Student’s two sample t-tests.

2.4 Stress fiber biochemistry

The contractile cytoskeleton is formed via the assembly of phosphorylated myosin and polymerized actin filaments to form contractile SFs. This process consists of three coupled phenomena: an activation signal which triggers the formation of the SFs, dissociation of fibers due to a reduction in tension, and a Hill type law relating the contractility of a SF to strain rate. Cellular signaling is represented here as an exponentially decaying signal $C = e^{(-t_1/\theta)}$, where θ is a constant that controls the decay rate of the signal and t_1 is the time since the most recent signal.

Cytoskeletal tension is essential for sustaining SF bundles and a reduction in tension below a defined isometric tension (σ_0) leads to fiber dissociation [27][28]. Fiber tension is generated by the cross-bridge cycling of actin-myosin pairs with a contractile behavior similar to that of skeletal muscle [29]. This behavior is captured using the following Hill-like relation between fiber stress (σ) and strain rate ($\dot{\varepsilon}$)

$$\frac{\sigma_f}{\sigma_0} = \begin{cases} 0 & \frac{\dot{\varepsilon}}{\dot{\varepsilon_0}} \le -\frac{\eta}{\overline{k_v}} \\ 1 + \frac{\overline{k_v}}{\eta}\frac{\dot{\varepsilon}}{\dot{\varepsilon_0}} & -\frac{\eta}{\overline{k_v}} \le \frac{\dot{\varepsilon}}{\dot{\varepsilon_0}} \le 0 \\ 1 & \frac{\dot{\varepsilon}}{\dot{\varepsilon_0}} > 0 \end{cases} \qquad (1)$$

where σ_f is the stress in the SF bundle, σ_0 is the isometric tension, $\overline{k_v}$ is the reduction in stress upon increasing the shortening rate, $\dot{\varepsilon}$, by $\dot{\varepsilon_0}$. The dimensionless activation level of a SF bundle, η, at any orientation also defines the isometric tension of the fiber in that orientation, σ_0, where $\sigma_0 = \eta\sigma_{max}$ and σ_{max} is the maximum tension in a fully activated SF.

The signal induced formation and tension dependent dissociation of the actin cytoskeleton is captured using a first order kinetic equation which gives the dimensionless activation level of a SF bundle, η:

$$\dot{\eta} = [1-\eta]\frac{Ck_f}{\theta} - \left[1 - \frac{\sigma}{\sigma_0}\right]\eta\frac{k_b}{\theta} \qquad (2)$$

where k_f and k_b are forwards and backwards reaction rates, C is an exponentially decaying signal, and θ is a decay constant.

This formulation is then implemented in a 3D environment as described by Ronan et al. [20]. In summary, a large number of fiber orientations (240) are considered at every point in the cell, as shown in Figure 2. A unit fiber along each orientation is given as $= sin(\omega)\,cos(\phi)\,\boldsymbol{x_1} + sin(\omega)\,sin(\phi)\,\boldsymbol{x_2} + cos(\omega)\,\boldsymbol{x_3}$, where ω and ϕ define the orientation of a fiber in 3D space; ω is the angle the fiber makes with the $\boldsymbol{x_3}$ axis and ϕ is the angle with the $\boldsymbol{x_1 x_2}$ plane. The strain rate for a given fiber $\dot{\varepsilon}$ is related to the material strain rate $\dot{\varepsilon}_{ij}$ by: $\dot{\varepsilon}_{ij} = cos^2(\varphi)sin^2(\omega)\dot{\varepsilon}_{11} + sin^2(\varphi)sin^2(\omega)\dot{\varepsilon}_{22} + cos^2(\omega)\dot{\varepsilon}_{33} + 2\varepsilon_{12}\cos\varphi\sin\varphi\sin^2\omega - 2\varepsilon_{23}\sin\omega\cos\omega\sin\varphi - 2\varepsilon_{13}\sin\omega\cos\omega\cos\varphi$. The active stress due to each fiber stress σ_f is calculated by summing over each direction:

$$\sigma_{ij}^A = \sum_{k=1}^{n} \frac{\sigma_f(\omega_k, \varphi_k)}{n} m(\omega_k, \varphi_k)_i m(\omega_k, \varphi_k)_j \qquad (3)$$

where n is the total number of directions. In addition to the active stress, the passive components of the cytoplasm are modeled as a neo-Hookean hyperelastic material and the passive stress is given as:

$$\sigma_{ij}^{P} = \frac{2}{J} C_{10} \left(\bar{B}_{ij} - \frac{1}{3} \bar{B}_{kk} \delta_{ij} \right) + \frac{2}{D_1} (J - 1) \qquad (4)$$

where $\bar{B}$ is the deviatoric left Cauchy-Green tensor and the elastic constants are given in terms of Young's modulus, E_c, and Poisson's ratio, ν_c, as:

$$C_{10} = \frac{E_c}{4(1+\nu_c)}, \qquad D_1 = \frac{6(1-2\nu_c)}{E_c} \qquad (5)$$

The active and passive formulations are implemented in parallel, as shown in Figure 2, in the finite element software Abaqus (SIMULIA, RI) as a user defined material. Finally, in order to visualize the resulting distributions of SFs, the SF variance Π gives the difference between the most highly activated SF and the average activation level.

$$\Pi = \eta_{max} - \bar{\eta} \qquad ; \qquad \bar{\eta} = \sum_{k=1}^{n} \frac{\eta_k}{n} \qquad (6)$$

The cell consists of two regions: the nucleus (shown in blue in Figure 2) is included as a separate hyperelastic material, and the cytoplasm consists of the active formulation in parallel with a passive hyperelastic material as described above. The two regions are continuous and no movement is permitted between the nucleus and cytoplasm

2.5 Simulating Cyto-D (treated) cells

Cells treated with cytochalasin-D are not contractile and are modeled as a passive hyperelastic material similarly to Eqn (4). Previous experimental observations suggest that the nucleus is 10 times stiffer than the cytoplasm; however, different values have been reported in other studies [9][30]. Three different ratios of nucleus stiffness to passive cell stiffness (5:1, 10:1, and 20:1) are considered in the present study. Cell geometries are assumed to be axisymmetric with cell and nucleus height and diameter being based on experimental measurements. Simulations of the passive elastic treated cells consist of a single load step during which the cell is compressed to 60 % of its original height. This corresponds to Part A of the material calibration, as shown in Figure 3.

2.6 Simulating untreated cells.

The active constitutive formulation is added to the cytoplasm material model used for passive cells. The nucleus is included as a separate hyperelastic material and all passive parameters (E_c, E_n, ν_c, ν_n) are kept the same as for passive cells. Cellular contractility is adjusted by varying σ_{max} and k_v. All other parameters for the active formulation are based on previous applications [20]. Simulations of untreated cells consist of two steps: in the first step SF growth is driven by an exponentially decaying signal. This leads to a change in the cell geometry whereby active contractility of the SFs reduce the height of the cell until an equilibrium is reached. This is shown as Part B in Figure 3. In the second step of the simulation the cell is compressed to 60 % of its equilibrium height, which is shown as Part C in Figure 3.

3 Results

3.1 Cell morphology change

The main geometrical characteristics of untreated and Cyto-D cells recorded from AFM measurements or stained cell analysis are reported in Table I. Analysis of AFM measurements showed cell height increased by 71 % ($p < 0.001$) and cell base area decreased by 29 % ($p < 0.001$) in response to Cyto-D treatment. Furthermore, analysis of stained cells showed the nucleus height increased by 57 % and nucleus diameter decrease by 41 % ($p < 0.01$) in response to Cyto-D treatment. It was also observed that the cytoplasm thickness above and below the nucleus increased by over 200 %.

From Figure 4, polymerized actin (red) was visible as long, linear bundles of filaments that transverse the cytoplasm of the cell surrounding the nucleus (blue) for untreated cells. Focal adhesions (vinculin) were observed as intense spots (green) at the terminal ends of actin filaments. This arrangement changed drastically due to the addition of Cyto-D. Actin depolymerized to its monomer form. This resulted in the disassembly of SFs and focal adhesions.

3.2 Monotonic compression

The mean experimental force versus compressive strain curves for untreated (blue) and Cyto-D (red) cells are shown in Figure 5. The raw AFM data used to derive this figure is provided as supplementary material (Figure S.1). Mean forces were calculated at compressive strain increments of 0.1. From Figure 5, it is evident that the force increased non-linearly with the imposed compressive strain in both cases. This behavior is more pronounced for the untreated cells. At 0.6 compressive strain, the mean maximum force recorded for the untreated cells is 936 ± 149 nN versus 511 ± 191 nN for the Cyto-D cells. This is a statistically significant difference ($p < 0.001$).

3.3 Simulated compression of passive (Cyto-D) cells (Calibration Part A)

Figure 6(A) shows the simulated reaction forces for a passive cell subjected to compression to 60 %. Reaction forces are shown for three different ratios of nucleus stiffness to cell stiffness: 5:1, 10:1, and 20:1. The nucleus stiffness was chosen such that reaction force at 60 % compression was equal to that obtained experimentally for cells treated with Cyto-D (~500 nN). This corresponds to a nucleus stiffness of 3.15 kPa, 4.5 kPa, and 6.3 kPa for E_n:E_c = 5:1;

10:1; and 20:1 respectively. It should be noted that the different ratios of E_n:E_c did not significantly alter the form of the force-strain curve.

The von Mises stress at a compressive strain of 0.6 is shown in Figure 6(B) for the different E_n:E_c ratios. Increasing the ratio E_n:E_c causes an increase in the cytoplasm stress directly above and below the nucleus; however the stress in the rest of the cytoplasm is significantly lower for all simulations. The stress in the nucleus is significantly larger than that in the cytoplasm, and increases with increasing E_n:E_c.

3.4 Cellular contractility (Calibration Part B)

SF distributions are shown in Figure 7 for different values of σ_{max}, k_v, and E_n:E_c at the end of the signal driven SF growth during the first step. Increasing the cellular contractility (higher σ_{max}) causes a higher SF variance (Π) throughout the cytoplasm. Increasing the slope of the Hill-curve (lower k_v) also leads to dominant bundles of SFs. Lowering k_v leads to a greater tension drop and therefore fibers that are shortening will dissociate faster. The lowest values of k_v and the highest value of σ_{max} causes the highest variance and, consequently, the greatest reduction of cytoplasm and nucleus height as a result of active SF contractility. Increasing the ratio of the nucleus to cytoplasm stiffness (E_n:E_c) leads to the formation of highly aligned dominant SFs and a larger reduction of the cell height. The ratio of 20:1 has the lowest cytoplasm stiffness (0.315 kPa) which provides less resistance to fiber contractility and hence the highest levels of SF dissociation as a result of tension reduction in the cytoplasm. The lower cytoplasm stiffness provides little support for SF tension, leading to a bigger drop in tension, and therefore more SF dissociation in certain directions. The SFs in the dominant direction will still have a high activation level, hence a higher SF variance is computed. In Figure 8, the effect of SF contractility on computed cell height at the end of the first step is shown. The height for a range of simulated cells with different values of σ_{max}, k_v, and E_n:E_c are presented. The starting cell height corresponds to the mean cell height for treated Cyto-D experimental cells and the target height corresponds to the mean cell height for active or untreated experimental cells (also indicated in Figure 8). Computed cell height is lowered by either decreasing σ_{max}, or decreasing k_v. Increasing E_n:E_c causes a small decrease in cell height. For each value of k_v and E_n:E_c, the value of σ_{max} that results in a reduction in cell height to the experimental target is identified in Table II. In summary, three pairings (σ_{max}, k_v) which correctly simulate the change in cell height due to SF contractility are identified for each E_n:E_c ratio.

3.5 Compression of contractile cells (Calibration Part C)

Using the nine possible (σ_{max}, k_v) pairings identified in Part B of the calibration above, cell compression is now simulated and results are compared to experimentally observed compression forces for untreated contractile cells. Computed compression forces at a compressive strain of 0.6 are shown in Figure 9. The reaction forces generated for k_v = 5 and k_v = 7 are ~5 and ~15 times larger than the experimentally observed value. The reaction forces for k_v = 2 are closer to the experimentally observed target. Furthermore, using a passive stiffness ratio of 5:1 and k_v = 2 gives the peak reaction force which is closest to the experimental value. This corresponds to a σ_{max} of 60 kPa and the passive stiffness of the cytoplasm and nucleus are 0.63 kPa and 3.15 kPa respectively.

In summary, in the first step of the computational investigation, as shown in Part A of Figure 3, three different ratios of E_n:E_c were initially simulated. In order to determine the correct level of nucleus stiffness for each ratio, these simulations were compared to the experimental compression forces observed for treated cells. Using these three selected values of passive cytoplasm and nucleus stiffness, in addition to the active parameters σ_{max} and k_v, the change in cell height between treated and untreated cells was simulated, as shown in Part B in Figure 3. For each value of nucleus stiffness identified in Part A of the calibration, 3 pairings of σ_{max} and k_v were obtained, giving 9 separate parameter sets. In the final step of the calibration, Part C in Figure 3, compression of untreated cells was performed using these 9 parameter sets. The computed compression results were then compared to the experimentally observed results to give the parameter set that provided the closest match. Thus, the parameter set that gives the best prediction of passive compression of treated cells and active compression and height change in untreated cells was selected.

Finally, the full compression force-strain curves using these parameters for the passive and active simulations are compared with experimental curves in Figure 10. The shape computational and experimental force strain curves are in very good agreement. However, the computed peak active force is higher than the experimental value.

3.6 Fiber orientation in irregularly shaped cells

In addition to the idealized axisymmetric cell geometry, an irregular cell geometry was constructed based on experimental images in order to directly compare predicted patterns of SF formation and orientation to experimental observations. The predicted dominant SF orientation is shown in Figure 11 for a simulation of the cell shown in Figure 4(B). In order to compare predicted SF distributions to the experimental data, a finite element model of an irregularly shaped cell is based on the experimentally observed dimensions of a single cell. The vectors in Figure 11 show the orientation of the most dominant SF at any given point in the cell cytoplasm. High levels of SF formation are predicted near the periphery of the cell, particularly in areas of high curvature, in strong agreement with the experimental image in Figure 4. SF orientation is also predicted in supplementary Figure S.2 for the cell shown in Figure 4(A). The simulated SF distribution in this cell is similar to the experimental observations at the periphery of the cell; however, the alignment of fibers in the area around the nucleus is not captured by the model.

4 Discussion

In the present study, it is demonstrated experimentally that the actin cytoskeleton plays a significant role in the resistance of osteoblasts to compression. Its removal results in a ~50 % decrease in the mean cell compression force compared to untreated control cells. Similar effects have been observed in an experimental study by Ofek et al. on chondrocytes, in which it was demonstrated that the actin cytoskeleton contributes more significantly to the resistance of cells to compression than intermediate filaments or microtubules [9]. Our results are also in broad agreement with the studies of Hofmann et al. on cardiocytes [31] and Rotsch and Radmacher on fibroblasts [32]. Using AFM probing of the cell surface, both studies report that untreated cells are ~3 times stiffer than cells treated with Cyto-D. In the present study it is also demonstrated that the contractility of the actin cytoskeleton has a pronounced effect on cell morphology. Both cell height and nucleus height increase significantly when the actin cytoskeleton is disrupted using Cyto-D. Cells appeared spindly and fragmented following Cyto-D treatment. A similar configuration was observed by Higuchi et al. following initial Cyto-D treatment of osteoblasts [33]. However, their study showed that the subsequent removal of Cyto-D resulted in cell morphology and cytoskeleton recovery, demonstrating that the osteoblasts are not adversely affected by Cyto-D treatment, despite their spindly and fragmented appearance.

The present study, for the first time, presents a detailed evaluation of the passive properties of the cytoplasm and nucleus and the active properties of the actin cytoskeleton. This evaluation is performed using experimental compression data for both untreated contractile osteoblasts and Cyto-D treated non-contractile osteoblasts. In order to determine the passive elastic components of the cytoplasm, we use compression data for cells in which active contractility has been removed. Following from this, observed changes in cell and nucleus height following disruption of cell contractility are used to uncover the contribution of SF contractility. Finally, compression data for untreated contractile cells are also used for the calibration in order to provide a unique set of active and passive properties for osteoblasts. As the calibration involves three interlinked steps, and exact match is only achieved for the first two steps, i.e., the compression of treated cells and the change in height between treated and untreated cells due SF contractility. The predicted compression forces for untreated cells, i.e. the third step of the calibration, are slightly higher than those observed experimentally; however, the model provides a very good approximation of the increase in compression resistance due to the presence of contractile SFs. An active bio-chemo-mechanical framework for SF remodeling and contractility is used to predict the distribution and contractility of the actin cytoskeleton and its contribution to cell morphology and compression resistance [17][20]. This approach to the interpretation of measured cell compression forces represents a considerable advance on previous studies, in which the cell cytoplasm is treated as a passive homogeneous hyperelastic or viscoelastic material [8][9][10]. Our experiments and simulations demonstrate that active contractility in osteoblasts contributes significantly to compression resistance.

The present study directly investigates the role of the actin cytoskeleton in the compression resistance of osteoblasts. Experimental compression of spread cells vary widely with cell type. Peak reaction forces at 70 % compression of 2500 nN are reported for highly contractile myoblasts [34], while lower forces are reported for less contractile cells: 500 nN for endothelial cells [8] and 360 nN for fibroblasts [35]. This trend suggests that highly contractile cells provide a greater resistance to applied compression. A recent computational investigation of the role of active SF assembly and contractility during cell compression reveals that the stretching of dominant fiber bundles during compression leads to a significant increase in the compression resistance of spread cells compared to round cells; this trend was observed for a number of different cell types and the increase in compression resistance was strongly dependent on the level cell contractility [20]. The compression value measured for osteoblasts in the current study (~900 nN at 60 % compression) is significantly higher than the aforementioned reported compression forces for endothelial cells and fibroblasts, suggesting that osteoblasts are highly contractile. The value of σ_{max} = 60 kPa determined for the active model used in the current study suggests that osteoblasts are highly contractile, and the largest change in cell height between treated and untreated cells was computed for this value of cell contractility. The higher level of contractility results in increased fiber tension leading to a lower steady state height being computed for untreated cells. In contrast, a recent study found that less contractile chondrocytes (σ_{max}= 0.85 kPa) show little change in cell height upon the addition of Cyto-D [36]. In comparison to the value of σ_{max} computed in the current study, a computational-experimental investigation of cells adhered to an array of microposts reports values of σ_{max} = 25 kPa, 12 kPa and 3.5 kPa for smooth muscle cells, MSCs and fibroblasts, respectively [19]. This investigation of cells adhered to microposts was performed using a previous 2-dimensional implementation of the constitutive formulation used in the current study, demonstrating the predictive capabilities of the formulation under different boundary conditions. While different boundary conditions will lead to different stress states and SF distributions in the cell, the formulation used in the current study has been shown to accurately simulate cells in compression [20], cells under shear [36], cells adhered to micropatterned islands [18], and cells adhered to continuous elastic substrates [37], using the same material parameters for each cell phenotype. The modeling framework used in the current study is entirely predictive and the material properties are not influenced by different boundary conditions.

The finding that the passive nucleus stiffness is five times higher than the passive cytoplasm properties differs from the predictions of Ofek et al. for chondrocytes [9]. However, it should be noted that Ofek et al. ignored the contribution of active SF contractility in the cytoplasm. The present study suggests that this omission would lead to an overestimation of the passive cytoplasm Young's modulus. The nucleus stiffness calibrated in the present study (~3 kPa) is similar to the stiffness of ~5 kPa reported by Caille et al. for isolated endothelial cell nuclei [8]. However, it is possible that removal of nuclei from the cell in the experiments of Caille et al. may alter their mechanical behavior. Interactions between the nucleus and cytoskeleton have been shown to significantly contribute to the mechanical regulation of the cell [37]. Furthermore, the removal of nuclear lamins leads to a significant decrease in the compressive strength of cells [38] and disruption of the actin cytoskeleton [39]. Knockdown of the nuclear protein nesprin-1 has also been shown to alter the cytoskeleton and inhibit cell reorientation under applied cyclic strain in endothelial cells [40].

Significant nucleus deformation due to SF contractility is observed in the present study. Similarly, in work of Avalos et al., nuclei in contractile cells are shown to be significantly flatter than spherical nuclei observed in treated Cyto-D cells [41]. In contrast to the present study, Avalos et al. did not implement force measurements in order to uncover the mechanical properties of the nucleus. Furthermore, the present study, for the first time, investigates the level of SF contractility required to generate correct nucleus deformed geometries in contractile spread cells. Results reveal that a ratio of maximum SF contractility to nucleus stiffness of ~20 predicts the correct level of nucleus deformation. Tension in SFs that are predicted to form over the nucleus flatten the nucleus, resulting in significant changes in nucleus height. In the current study, the nucleus has been simulated as a homogenous hyperelastic material. However, previous studies have shown that isolated nuclei exhibit a viscoelastic response [42] and that the nucleus is not a homogenous body [43]. In the current study, the nucleus and the cytoplasm are simulated as two separate but continuous regions; however, nuclear binding proteins are not explicitly included. It should be noted that no movement is permitted between the cell and nucleus, which represents a uniform distribution of rigid nesprins. Also, other components of the cytoplasm, such as microtubules and intermediate filaments, have been included in the current study as part of the homogenous passive material which is in parallel with the active SF component.

The constitutive formulation employed in the current study predicts the distribution and contractility of the actin cytoskeleton in spread cells. However, the spreading process itself has been shown to influence SF distribution and lead to the formation of fiber bundles leading from the cell periphery over the nucleus [44]. In the current study, simulations of treated and untreated cells to determine the change in cell height and compression resistance of cells were performed using axisymmetric finite element meshes. Axisymmetry has been used previously to simulate the compression [8][45] and micropipette aspiration of cells [43][46]. A previous computational investigation of cell compression predicted different SF distributions in axisymmetric and polarized cell geometries; however, both geometries were found to contain SFs that were stretched during compression, providing increased resistance to compression [20]. In the current study, an irregularly shaped cell was simulated in order to directly compare predicted SF distributions to experimental observations. The orientation and location of dominant SFs bundles in the simulations and experiments were in strong agreement, particularly for SFs parallel to the cell edge. In cells with an approximately axisymmetric geometry and displaying SFs oriented in a dominant direction across the cell, the SF model fails to capture the orientation of fibres around the nucleus. This discrepancy may be due to a number of factors, including difficulty in accurately modelling the cell geometry and any anisotropy that may have been introduced during the spreading process. However, the model predictions are in good agreement in regions where the cell edge is smoother.

Rate dependent viscoelasticity was not considered for the passive components of the cell and the cell nucleus in the current study as only one compression velocity was considered. Further experiments should be performed over a wide range of loading rates in order to characterize the rate dependent viscoelasticity of the cell and nucleus. The compression velocity used in the current study is in the same range to that used by Caille et al. (0.25 µm/s) [8] and Peeters et al. (0.40 µm/s) [34]. In both of these studies, cell viscoelasticity was not considered and the cell material was simulated using a passive hyperelastic formulation. In the dynamic compression experiments of Peeters et al. a wide range of compression velocities ranging from 0.1 - 20 µm/s was investigated, requiring the use of a passive viscoelastic material model [10]. Cytoplasm viscoelasticity has also been considered in the simulation of dynamic stretching of cells [47].

In summary, the present study combines experimental compression techniques with active modeling of the cell actin cytoskeleton. A full calibration of passive mechanical properties in parallel with active SF contractility parameters is performed for osteoblasts. It is demonstrated that osteoblasts are highly contractile and that significant changes to the cell and nucleus geometries occur when SF contractility is removed. Future investigations should include the seeding of osteoblasts on arrays of microposts in order to validate the high levels of contractility predicted by the present simulations.

Acknowledgements

This work was supported by Science Foundation Ireland (Grant No. 08/RFP/ENM1726), the Irish Research Council for Science and Engineering Technology, and the Irish Centre for High End Computing.

Figure and Table Captions

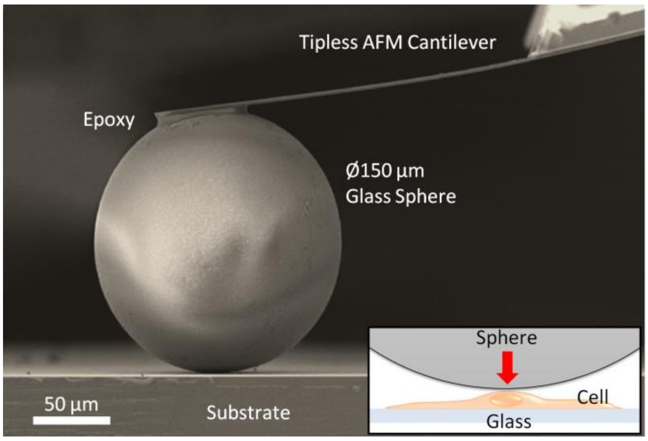
Tipless AFM Cantilever
Epoxy
Ø150 µm
Glass Sphere
50 µm
Substrate
Sphere
Cell
Glass

Figure 1 – Modified-AFM cantilever: a Ø 150 µm glass microsphere is attached to the edge of an AFM tipless cantilever. The bottom surface of the sphere is brought into contact with a cell and then applies a whole cell deformation when the cantilever is moved downwards (see inset schematic). As the diameter of the sphere is significantly larger than the contact zone it provides a close approximation to parallel plate compression.

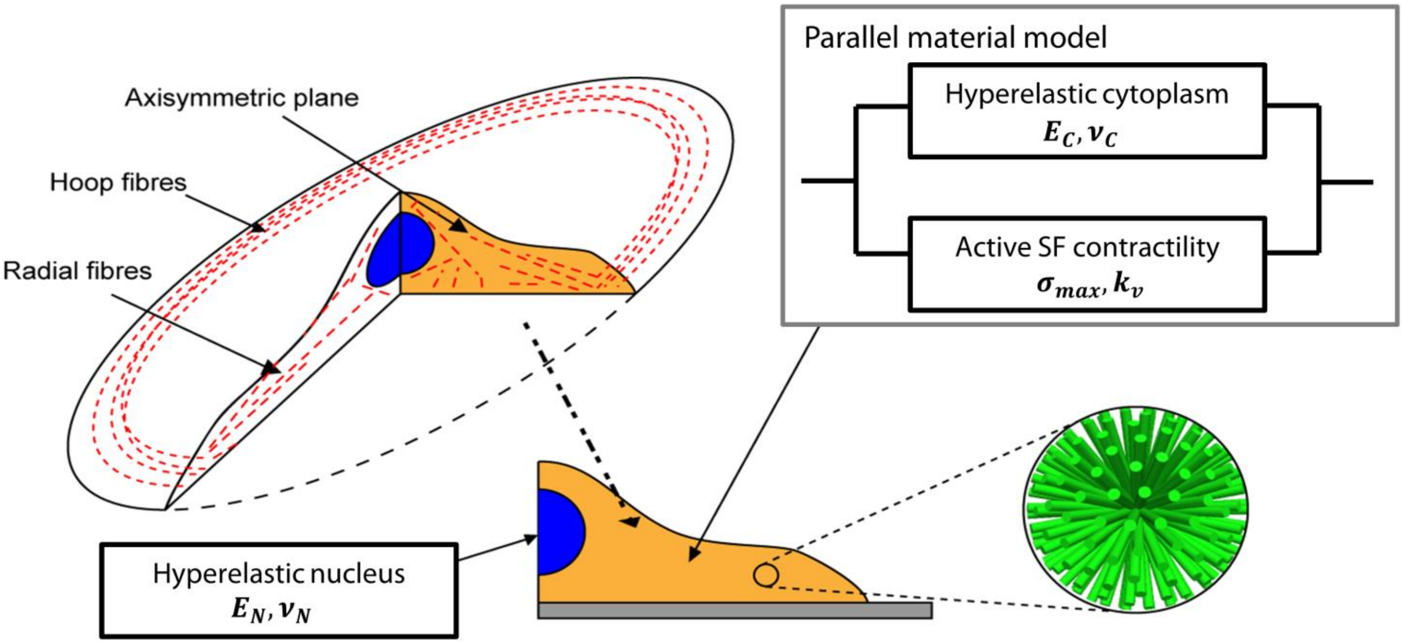
Axisymmetric plane
Hoop fibres
Radial fibres
Parallel material model
Hyperelastic cytoplasm
E_C, ν_C
Active SF contractility
σ_{max}, k_v
Hyperelastic nucleus
E_N, ν_N

Figure 2 – Schematic diagram of an axisymmetric cell, showing the axisymmetric plane in detail. The exploded view shows the 3D orientation of fiber directions (n = 240) at every integration point. The nucleus is modeled as a hyperelastic material. The cytoplasm is modeled as a hyperelastic material in parallel with active SF contractility.

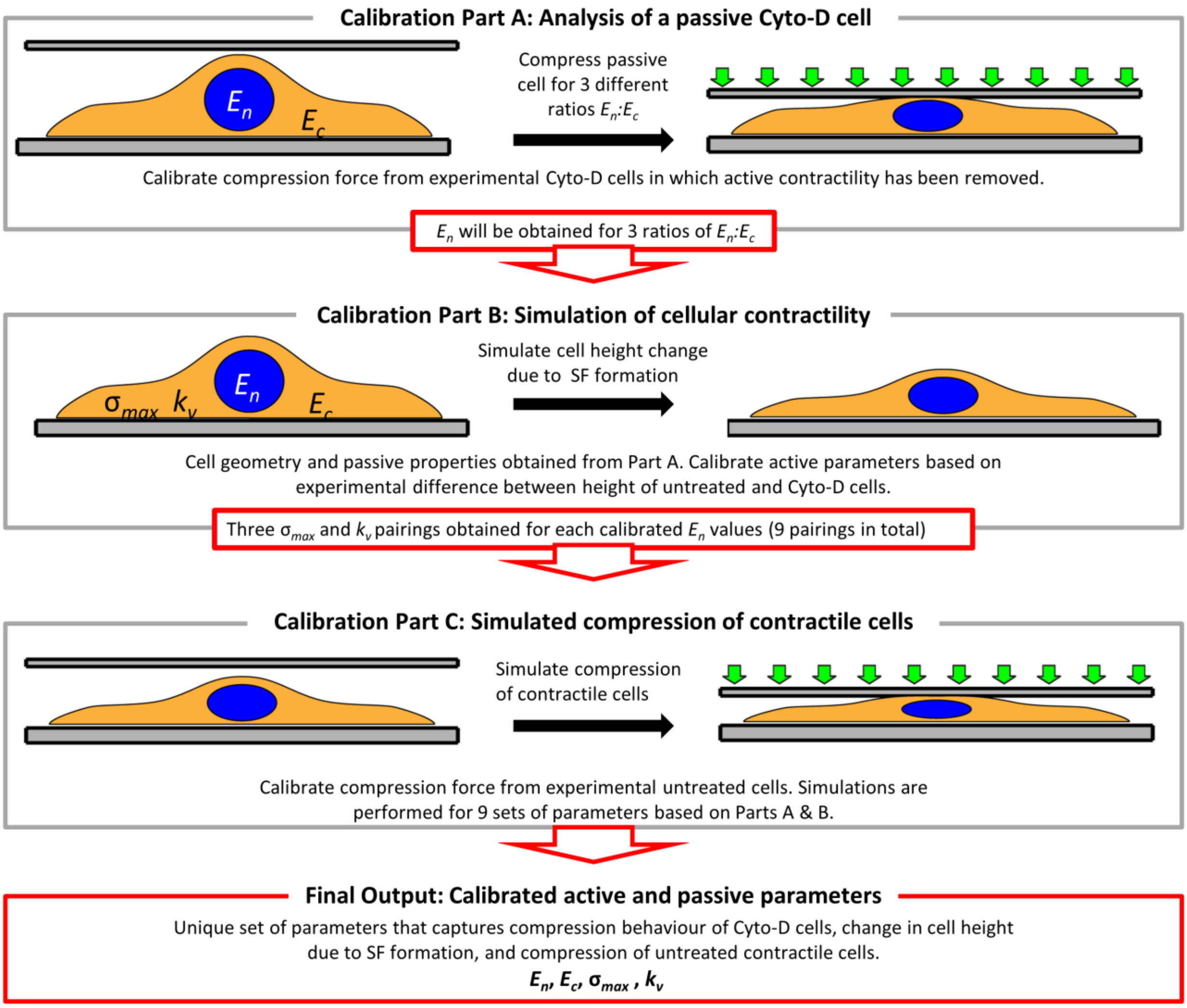
Calibration Part A: Analysis of a passive Cyto-D cell
E_n
E_c
Compress passive cell for 3 different ratios E_n:E_c
Calibrate compression force from experimental Cyto-D cells in which active contractility has been removed.
E_n will be obtained for 3 ratios of E_n:E_c
Calibration Part B: Simulation of cellular contractility
σ_{max} k_v
E_n
E_c
Simulate cell height change due to SF formation
Cell geometry and passive properties obtained from Part A. Calibrate active parameters based on experimental difference between height of untreated and Cyto-D cells.
Three σ_{max} and k_v pairings obtained for each calibrated E_n values (9 pairings in total)
Calibration Part C: Simulated compression of contractile cells
Simulate compression of contractile cells
Calibrate compression force from experimental untreated cells. Simulations are performed for 9 sets of parameters based on Parts A & B.
Final Output: Calibrated active and passive parameters
Unique set of parameters that captures compression behaviour of Cyto-D cells, change in cell height due to SF formation, and compression of untreated contractile cells.
E_n, E_c, σ_{max}, k_v

Figure 3 – Flowchart showing simulations performed to calibrate the active and passive material models.

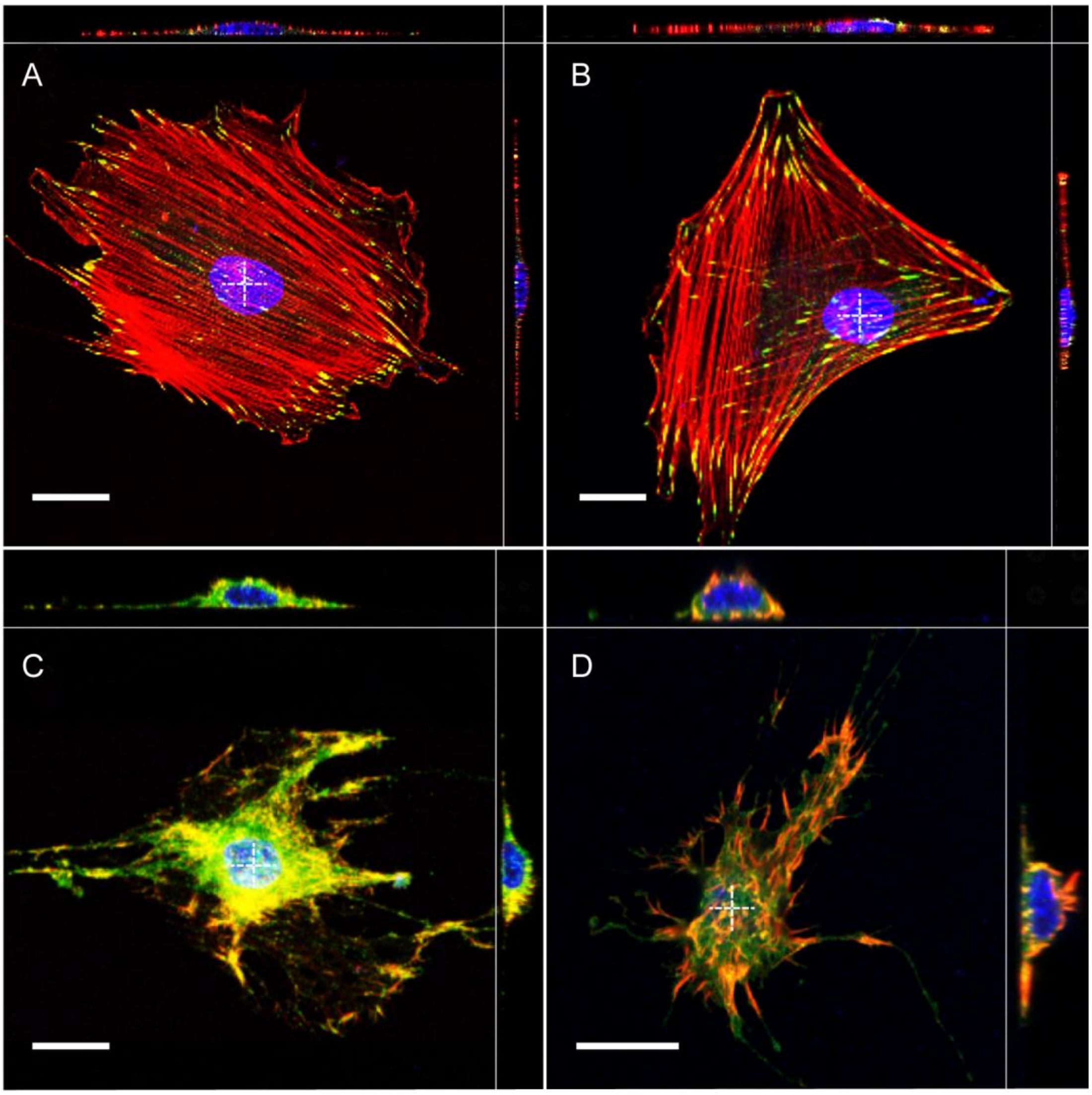

Figure 4 – Stained cell images of untreated (A, B) and Cyto-D (C, D) cells. Cells were stained for actin (red), vinculin (green) and nuclei (blue). Section views were taken across the nucleus center (dashed lines) in all cases. Scale bar = 20 µm.

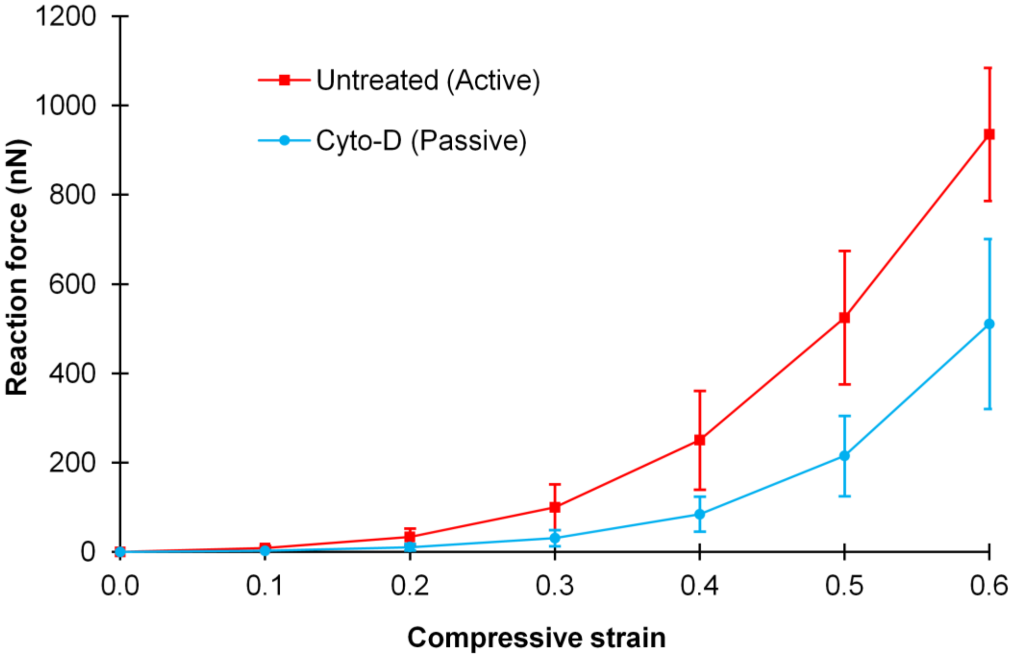

Figure 5 – Reaction force versus compressive strain curves (mean ± SD) obtained experimentally for untreated cells (red) and Cyto-D (blue) cells.

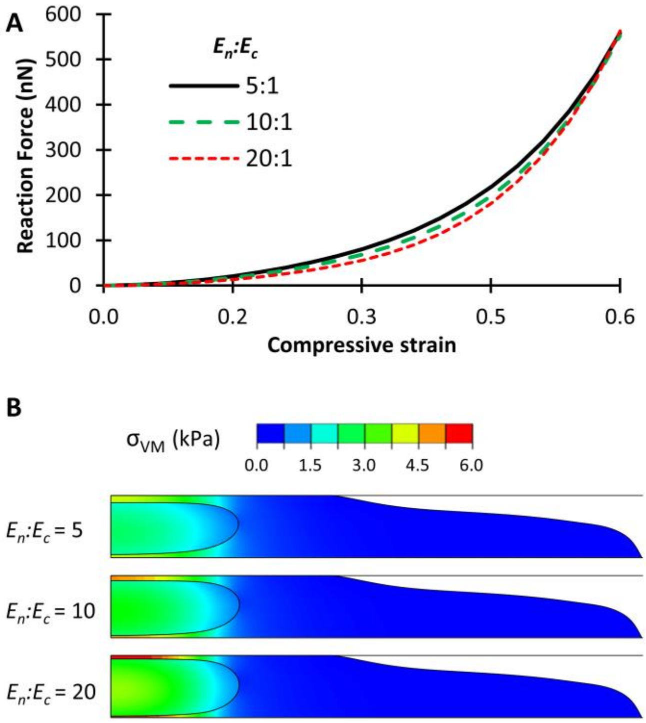

Figure 6 – (A) Simulated compression reaction forces (nN) in passive cells for three different ratios of nucleus stiffness to cytoplasm stiffness (E_n:E_c). (B) Von Mises stress (σ_{VM}) in the cell for each ratio E_n:E_c.

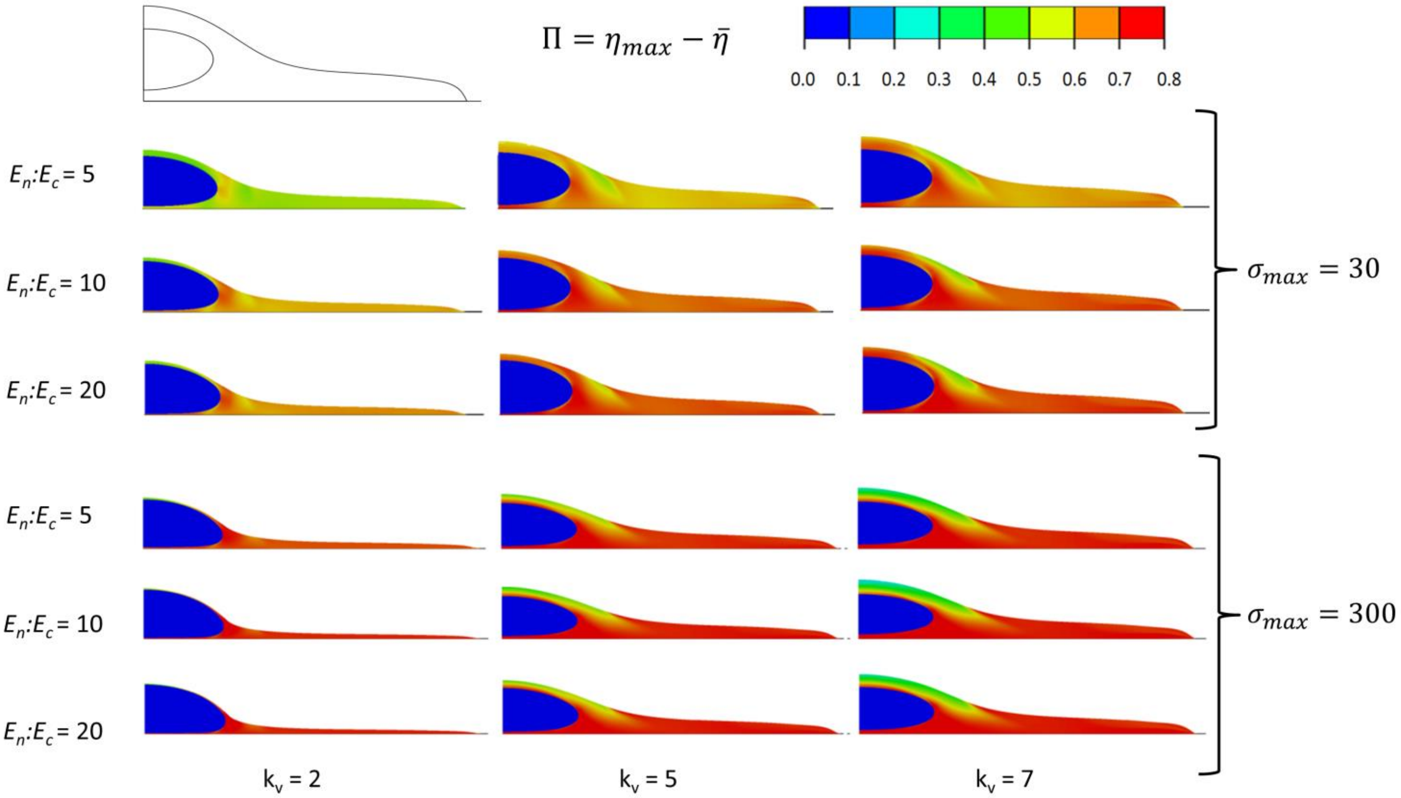

Figure 7 – Computed stress fiber variance (Π) in each contractile cell shows where fibers have aligned in a dominant orientation to form a large stress fiber bundle. The variance is shown for 3 different values of k_v and E_n:E_c, and for both a high and low value of σ_{max}.

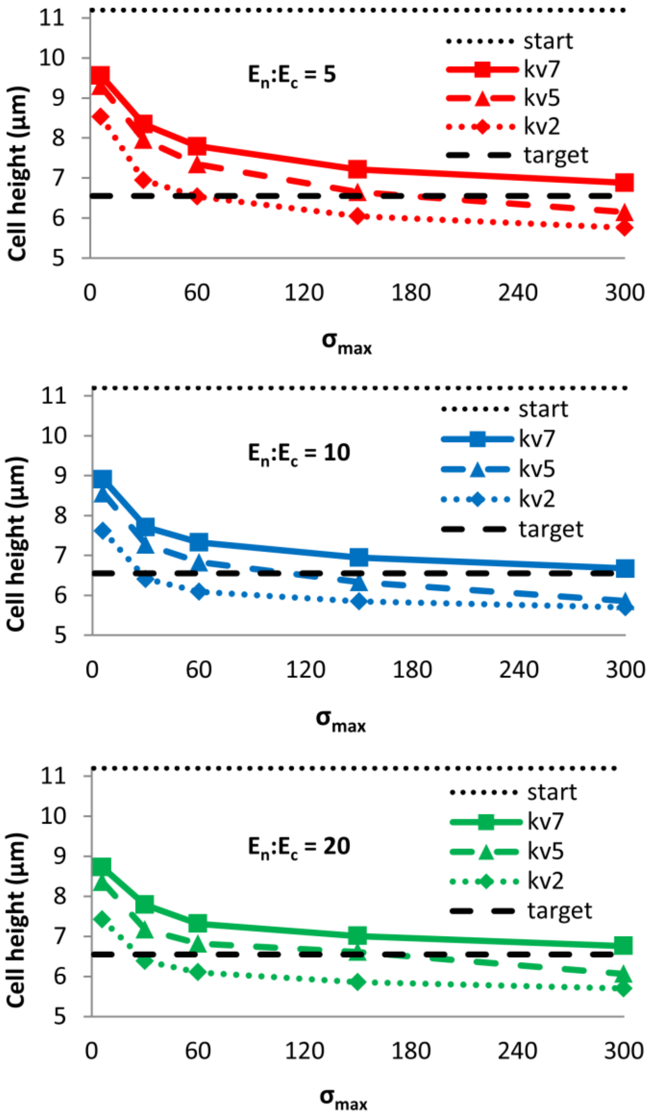

Figure 8 – Simulated cell height after the addition of cellular contractility. Heights are shown for different values of k_v and σ_{max} and for different ratios of nucleus to cell stiffness (A-C). The starting height of the cell (dotted line) is the experimentally observed mean height for treated cells. The target cell height (dashed line) is the experimentally observed mean height for untreated cells.

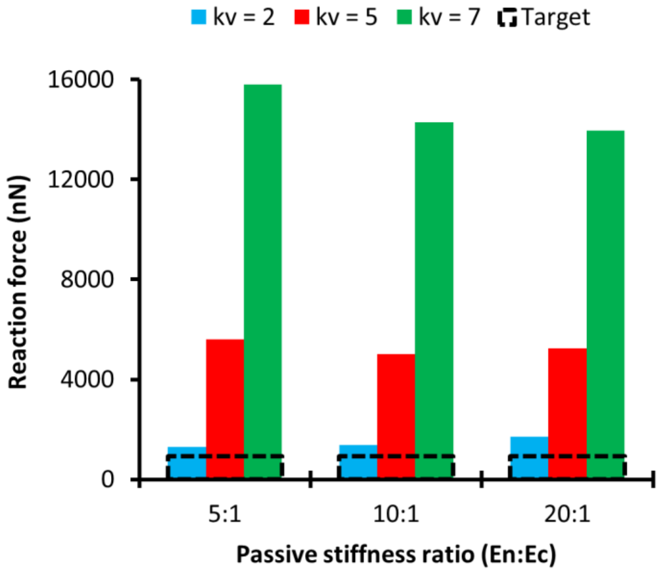

Figure 9 – Simulated reaction forces at 60 % compression for different values of k_v and E_n:E_c. For each simulation, σ_{max} is chosen to give the correct reduction in cell height after the addition of contractility. The experimentally observed mean reaction force at 60 % compression is shown as a dotted line.

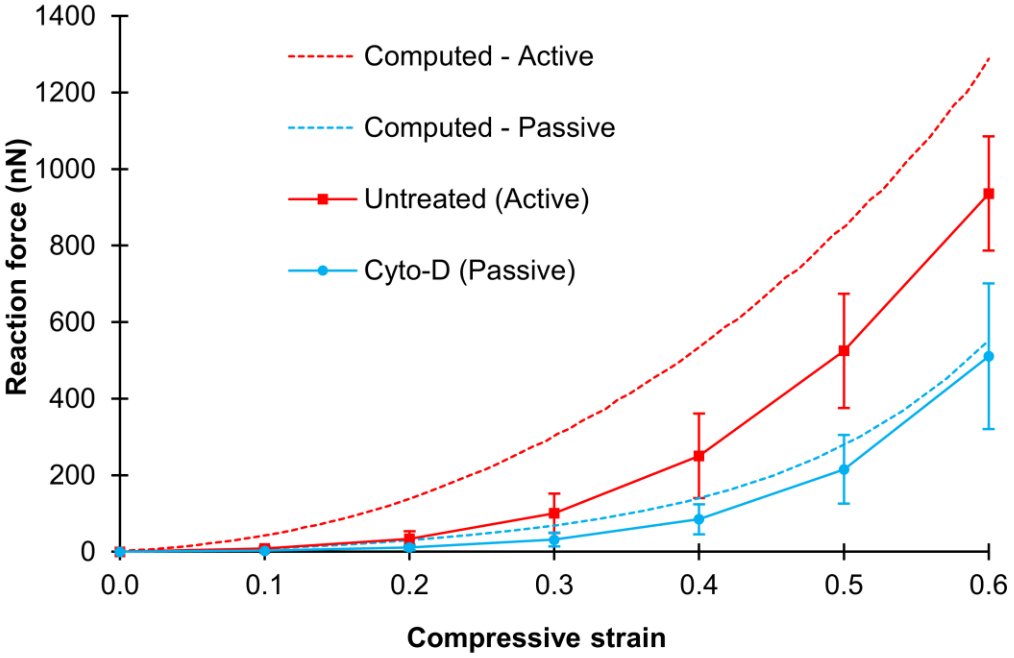

Figure 10 – Simulated (dashed lines) and experimental (solid lines) reaction forces for active/untreated (red) and passive/treated (blue) cells. Experimental curves show the mean ± standard deviation.

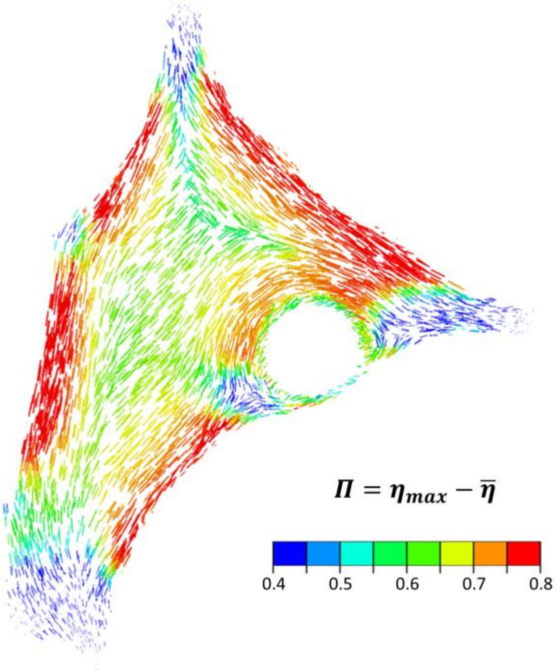

Figure 11 – Predicted SF (stress fiber) orientation in an irregularly shaped cell (the corresponding experimental image is shown in Figure 4(B)). The computed orientation and activation level of the dominant fiber at each point is shown by the vector direction and length. The SF variance Π is shown via the colour of the vectors.

Table I – Cell geometry characteristics for untreated and Cyto-D cells (mean ± standard deviation).

	Untreated	Cyto-D	% Change of Mean Values
Cell height (µm)	6.3 ± 2.49	10.8 ± 2.78	71.40%
Cell base area (µm^2)	3898 ± 1776	2776 ± 1824	-28.80%
Nucleus Height (µm)	4.6 ± 0.8	7.2 ± 3.0	56.50%
Nucleus Diameter (µm)	25.6 ± 4.9	15.1 ± 2.4	-41.00%
Cytoplasm above nucleus (µm)	0.7 ± 0.5	2.7 ± 2.0	285.70%
Cytoplasm below nucleus (µm)	0.4 ± 0.3	1.3 ± 1.0	225.00%

Table II – Calibrated values of σ_{max} for three different values of k_v and three different passive stiffness ratios E_n:E_c.

	k_v = 2	k_v = 5	k_v = 7
E_n:E_c =5	60 kPa	150 kPa	300 kPa
E_n:E_c = 10	30 kPa	150 kPa	300 kPa
E_n:E_c = 20	30 kPa	150 kPa	300 kPa

References

1. H. M. Frost (2004), A 2003 update of bone physiology and wolff's law for clinicians, The Angle Orthodontist, 74 (1), 3-15.
2. R. Duncan and C. Turner (1995), Mechanotransduction and the functional response of bone to mechanical strain, Calcified tissue international, 57 (5), 344-358.
3. I. Owan, D. B. Burr, C. H. Turner, J. Qiu, Y. Tu, J. E. Onyia and R. L. Duncan (1997), Mechanotransduction in bone: Osteoblasts are more responsive to fluid forces than mechanical strain, American Journal of Physiology-Cell Physiology, 273 (3), C810-C815.
4. J. S. Gabbay, P. A. Zuk, A. Tahernia, M. Askari, C. M. O'Hara, T. Karthikeyan, K. Azari, J. O. Hollinger and J. P. Bradley (2006), In vitro microdistraction of preosteoblasts: Distraction promotes proliferation and oscillation promotes differentiation, Tissue engineering, 12 (11), 3055-3065.
5. B. Rath, J. Nam, T. J. Knobloch, J. J. Lannutti and S. Agarwal (2008), Compressive forces induce osteogenic gene expression in calvarial osteoblasts, Journal of Biomechanics, 41 (5), 1095-1103.
6. A. C. Shieh and K. A. Athanasiou (2007), Dynamic compression of single cells, Osteoarthritis and Cartilage, 15 (3), 328-334.
7. O. Thoumine, O. Cardoso and J. J. Meister (1999), Changes in the mechanical properties of fibroblasts during spreading: A micromanipulation study, European Biophysics Journal with Biophysics Letters, 28 (3), 222-234.
8. N. Caille, O. Thoumine, Y. Tardy and J. J. Meister (2002), Contribution of the nucleus to the mechanical properties of endothelial cells, Journal of Biomechanics, 35 (2), 177-187.
9. G. Ofek, R. M. Natoli and K. A. Athanasiou (2009), In situ mechanical properties of the chondrocyte cytoplasm and nucleus, Journal of Biomechanics, 42 (7), 873-877.
10. E. A. Peeters, C. W. Oomens, C. V. Bouten, D. L. Bader and F. P. Baaijens (2005), Viscoelastic properties of single attached cells under compression, Journal of Biomechanical Engineering, 127 (2), 237-243.
11. V. Lulevich, T. Zink, H.-Y. Chen, F.-T. Liu and G.-y. Liu (2006), Cell mechanics using atomic force microscopy-based single-cell compression, Langmuir, 22 (19), 8151-8155.
12. E. M. Darling, M. Topel, S. Zauscher, T. P. Vail and F. Guilak (2008), Viscoelastic properties of human mesenchymally-derived stem cells and primary osteoblasts, chondrocytes, and adipocytes, Journal of Biomechanics, 41 (2), 454-464.

13. J. P. McGarry and P. E. McHugh (2008), Modelling of in vitro chondrocyte detachment, Journal of the Mechanics and Physics of Solids, 56 (4), 1554-1565.
14. J. P. McGarry (2009), Characterization of cell mechanical properties by computational modeling of parallel plate compression, Annals of Biomedical Engineering, 37 (11), 2317-2325.
15. C. Mohrdieck, A. Wanner, W. Roos, A. Roth, E. Sackmann, J. P. Spatz and E. Arzt (2005), A theoretical description of elastic pillar substrates in biophysical experiments, Chemphyschem, 6 (8), 1492-1498.
16. C. Storm, J. J. Pastore, F. C. MacKintosh, T. C. Lubensky and P. A. Janmey (2005), Nonlinear elasticity in biological gels, Nature, 435 (7039), 191-194.
17. V. S. Deshpande, R. M. McMeeking and A. G. Evans (2007), A model for the contractility of the cytoskeleton including the effects of stress-fibre formation and dissociation, Proceedings of the Royal Society A: Mathematical, Physical and Engineering Science, 463 (2079), 787-815.
18. A. Pathak, V. S. Deshpande, R. M. McMeeking and A. G. Evans (2008), The simulation of stress fibre and focal adhesion development in cells on patterned substrates, Journal of The Royal Society Interface, 5 (22), 507-524.
19. J. P. McGarry, J. Fu, M. T. Yang, C. S. Chen, R. M. McMeeking, A. G. Evans and V. S. Deshpande (2009), Simulation of the contractile response of cells on an array of micro-posts, Philosophical Transactions of the Royal Society a-Mathematical Physical and Engineering Sciences, 367 (1902), 3477-3497.
20. W. Ronan, V. S. Deshpande, R. M. McMeeking and J. P. McGarry (2012), Numerical investigation of the active role of the actin cytoskeleton in the compression resistance of cells, Journal of the Mechanical Behavior of Biomedical Materials, 14, 143-157.
21. P. Weafer, J. McGarry, M. van Es, J. Kilpatrick, W. Ronan, D. Nolan and S. Jarvis (2012), Stability enhancement of an atomic force microscope for long-term force measurement including cantilever modification for whole cell deformation, Review of Scientific Instruments, 83 (9), 093709-093709-10.
22. V. S. Deshpande, R. M. McMeeking and A. G. Evans (2006), A bio-chemo-mechanical model for cell contractility, Proceedings of the National Academy of Sciences, 103 (38), 14015-14020.
23. J. P. Cleveland, S. Manne, D. Bocek and P. K. Hansma (1993), A nondestructive method for determining the spring constant of cantilevers for scanning force microscopy, Review of Scientific Instruments, 64 (2), 403-405.
24. H. J. Butt and M. Jaschke (1995), Calculation of thermal noise in atomic force microscopy, Nanotechnology, 6 (1), 1-7.

25. J. G. McGarry, P. Maguire, V. A. Campbell, B. C. O'Connell, P. J. Prendergast and S. P. Jarvis (2008), Stimulation of nitric oxide mechanotransduction in single osteoblasts using atomic force microscopy, Journal of Orthopaedic Research, 26 (4), 513-521.
26. G. M. Kelly, J. I. Kilpatrick, M. H. van Es, P. P. Weafer, P. J. Prendergast and S. P. Jarvis (2011), Bone cell elasticity and morphology changes during the cell cycle, Journal of Biomechanics, 44 (8), 1484-1490.
27. R. P. Franke, M. Grafe, H. Schnittler, D. Seiffge, C. Mittermayer and D. Drenckhahn (1984), Induction of human vascular endothelial stress fibres by fluid shear stress, Nature, 307 (5952), 648-649.
28. J. Kolega (1986), Effects of mechanical tension on protrusive activity and microfilament and intermediate filament organization in an epidermal epithelium moving in culture, Journal of Cell Biology, 102 (4), 1400-1411.
29. D. M. Warshaw, J. M. Desrosiers, S. S. Work and K. M. Trybus (1990), Smooth muscle myosin cross-bridge interactions modulate actin filament sliding velocity in vitro, Journal of Cell Biology, 111 (2), 453-463.
30. F. Guilak and V. C. Mow (2000), The mechanical environment of the chondrocyte: A biphasic finite element model of cell-matrix interactions in articular cartilage, Journal of Biomechanics, 33 (12), 1663-1673.
31. U. G. Hofmann, C. Rotsch, W. J. Parak and M. Radmacher (1997), Investigating the cytoskeleton of chicken cardiocytes with the atomic force microscope, Journal of Structural Biology, 119 (2), 84-91.
32. C. Rotsch and M. Radmacher (2000), Drug-induced changes of cytoskeletal structure and mechanics in fibroblasts: An atomic force microscopy study, Biophysical Journal, 78 (1), 520-535.
33. C. Higuchi, N. Nakamura, H. Yoshikawa and K. Itoh (2009), Transient dynamic actin cytoskeletal change stimulates the osteoblastic differentiation, Journal of bone and mineral metabolism, 27 (2), 158-167.
34. E. A. Peeters, C. W. Oomens, C. V. Bouten, D. L. Bader and F. P. Baaijens (2005), Mechanical and failure properties of single attached cells under compression, Journal of Biomechanics, 38 (8), 1685-1693.
35. Z. Deng, V. Lulevich, F.-t. Liu and G.-y. Liu (2010), Applications of atomic force microscopy in biophysical chemistry of cells, The Journal of Physical Chemistry B, 114 (18), 5971-5982.
36. E. P. Dowling, W. Ronan, G. Ofek, V. S. Deshpande, K. A. Athanasiou, R. M. McMeeking and J. P. McGarry (2012), The effect of remodelling and contractility of the actin cytoskeleton on the shear resistance of single cells: A computational and experimental investigation, Journal of The Royal Society Interface, 9 (77), 3469-3479.
37. F. Houben, F. C. S. Ramaekers, L. H. E. H. Snoeckx and J. L. V. Broers (2007), Role of nuclear lamina-cytoskeleton interactions in the maintenance of cellular strength, Biochimica et Biophysica Acta (BBA) - Molecular Cell Research, 1773 (5), 675-686.

38. J. L. V. Broers, E. A. G. Peeters, H. J. H. Kuijpers, J. Endert, C. V. C. Bouten, C. W. J. Oomens, F. P. T. Baaijens and F. C. S. Ramaekers (2004), Decreased mechanical stiffness in lmna−/− cells is caused by defective nucleo-cytoskeletal integrity: Implications for the development of laminopathies, Human Molecular Genetics, 13 (21), 2567-2580.
39. S. B. Khatau, C. M. Hale, P. J. Stewart-Hutchinson, M. S. Patel, C. L. Stewart, P. C. Searson, D. Hodzic and D. Wirtz (2009), A perinuclear actin cap regulates nuclear shape, Proceedings of the National Academy of Sciences, 106 (45), 19017-19022.
40. T. Chancellor, J. Lee, C. K. Thodeti and T. Lele (2010), Actomyosin tension exerted on the nucleus through nesprin-1 connections influences endothelial cell adhesion, migration, and cyclic strain-induced reorientation, Biophysical Journal, 99 (1), 115-123.
41. P. G. Avalos, M. Reichenzeller, R. Eils and E. Gladilin (2011), Probing compressibility of the nuclear interior in wild-type and lamin deficient cells using microscopic imaging and computational modeling, Journal of Biomechanics, 44 (15), 2642-2648.
42. F. Guilak, J. R. Tedrow and R. Burgkart (2000), Viscoelastic properties of the cell nucleus, Biochemical and Biophysical Research Communications, 269 (3), 781-786.
43. A. C. Rowat, L. J. Foster, M. M. Nielsen, M. Weiss and J. H. Ipsen (2005), Characterization of the elastic properties of the nuclear envelope, Journal of The Royal Society Interface, 2 (2), 63-69.
44. W. Ronan, V. S. Deshpande, R. M. McMeeking and J. P. McGarry, (2011), Simulation of stress fiber remodeling and mixed mode focal adhesion assembly during cell spreading and for cells adhered to elastic substrates, Proceedings of the ASME 2011 Summer Bioengineering Conference, Farmington, PA, USA, SBC2011-53878.
45. G. Ofek, D. C. Wiltz and K. A. Athanasiou (2009), Contribution of the cytoskeleton to the compressive properties and recovery behavior of single cells, Biophysical Journal, 97 (7), 1873-1882.
46. M. A. Haider and F. Guilak (2002), An axisymmetric boundary integral model for assessing elastic cell properties in the micropipette aspiration contact problem, Journal of Biomechanical Engineering, 124 (5), 586-595.
47. J. P. McGarry, B. P. Murphy and P. E. McHugh (2005), Computational mechanics modelling of cell-substrate contact during cyclic substrate deformation, Journal of the Mechanics and Physics of Solids, 53 (12), 2597-2637.